

Modulated reconstruction by epitaxial strain engineering and chemical arrangement in $SrNbO_3$ thin films

Shenggen Cao(曹声根), Jiali Zhao(赵佳丽), Hang Li(李航), and Tian Qian(钱天)
Citation: Chin. Phys. B, 2026, 35 (**7**): 076802. DOI: 10.1088/1674-1056/ae5a0b
http://cpb.iphy.ac.cn; http://iopscience.iop.org/cpb

What follows is a list of articles you may be interested in

Bond-resolved silicene on Au(111) substrate

Ye Chen(陈烨), Wenya Zhai(翟文雅), Haoyuan Zang(臧浩原), Zengfu Ou(欧增福), Donghui Guo(郭东辉), and Jingcheng Li(李竟成)
Chin. Phys. B, 2025, 34 (**9**): 096801. DOI: 10.1088/1674-1056/adee02

Combining machine learning algorithms with traditional methods for resolving the atomic-scale dynamic structure of monolayer MoS_2 in high-resolution transmission electron microscopy

Yu Meng(蒙宇), Shuya Wang(王淑雅), Xibiao Ren(任锡标), Han Xue(薛涵), Xuejun Yue(岳学军), Chuanhong Jin(金传洪), Shanggang Lin(林上港), and Fang Lin(林芳)
Chin. Phys. B, 2025, 34 (**1**): 016802. DOI: 10.1088/1674-1056/ad9ba3

Multiphase cooperation for multilevel strain accommodation in a single-crystalline $BiFeO_3$ thin film

Wooseon Choi, Bumsu Park, Jaejin Hwang, Gyeongtak Han, Sang-Hyeok Yang, Hyeon Jun Lee, Sung Su Lee, Ji Young Jo, Albina Y. Borisevich, Hu Young Jeong, Sang Ho Oh, Jaekwang Lee, and Young-Min Kim
Chin. Phys. B, 2024, 33 (**9**): 096805. DOI: 10.1088/1674-1056/ad62e0

Optimal parameter space for stabilizing the ferroelectric phase of $Hf_{0.5}Zr_{0.5}O_2$ thin films under strain and electric fields

Lvjin Wang(王侣锦), Cong Wang(王聪), Linwei Zhou(周霖蔚), Xieyu Zhou(周谐宇), Yuhao Pan(潘宇浩), Xing Wu(吴幸), and Wei Ji(季威)
Chin. Phys. B, 2024, 33 (**7**): 076803. DOI: 10.1088/1674-1056/ad498b

Quantum dynamics within curved thin layers with deviation

Run Cheng(程润), Hao Zhao(赵浩), Cui-Bai Luo(罗翠柏), Xuan Zhou(周璇), Bi-Li Wang(王必利), Yan-Biao Li(李延标), and Jun Wang(王骏)
Chin. Phys. B, 2024, 33 (**7**): 076801. DOI: 10.1088/1674-1056/ad3dd2

RAPID COMMUNICATION

Modulated reconstruction by epitaxial strain engineering and chemical arrangement in $SrNbO_3$ thin films

Shenggen Cao(曹声根)[1,2], Jiali Zhao(赵佳丽)[1,2], Hang Li(李航)[1,2,†], and Tian Qian(钱天)[1,2,3]

[1] *Beijing National Laboratory for Condensed Matter Physics, Institute of Physics, Chinese Academy of Sciences, Beijing* 100190, *China*
[2] *University of Chinese Academy of Sciences, Beijing* 100049, *China*
[3] *CAS Center for Excellence in Topological Quantum Computation, Chinese Academy of Sciences, Beijing* 100049, *China*

(Received 7 January 2026; revised manuscript received 20 March 2026; accepted manuscript online 1 April 2026)

Correlated topological quantum materials hold great promise for next-generation quantum technologies, particularly in fault-tolerant quantum computing and energy-efficient spintronic devices, owing to the intricate interplay between strong electron correlations and topologically nontrivial band structures. To experimentally probe correlation-driven band reconstruction, perovskite oxide heterostructures provide an ideal platform, as their epitaxial films offer versatile degrees of freedom for physical modulation through strain or chemical control. In this work, we systematically fabricate high-quality $SrNbO_3$ thin films via pulsed laser epitaxy and investigate their electronic structures using angle-resolved photoemission spectroscopy (ARPES). Variation of the substrate oxygen stoichiometry drives a transition in the Fermi surface reconstruction from a $\sqrt{2}\times\sqrt{2}R45^\circ$ pattern on oxygen-deficient $SrTiO_3$ to a 2×2 pattern on stoichiometric substrates. Furthermore, by precisely controlling the epitaxial thickness, we identify the gradual disappearance of the electron-like Fermi surface at the M point with increasing thickness, which might be associated with the relaxation of the $a^0a^0c^+$ lattice distortion induced by interfacial epitaxial strain at the $SrTiO_3$ substrate. Our findings demonstrate that band reconstruction in correlated oxides can be effectively modulated through chemistry and thin-film thickness, establishing $SrNbO_3$ as a promising material platform for multifunctional electronic band control. This work provides a prototypical route for exploring the intertwined topological and correlated phenomena in 4d transition-metal oxides under extreme quantum confinement.

Keywords: perovskite oxide, strain, reconstruction

PACS: 68.47.Gh, 71.10.Ca, 73.20.–r, 73.22.–f

DOI: 10.1088/1674-1056/ae5a0b **CSTR:** 32038.14.CPB.ae5a0b

1. Introduction

Transition-metal-based perovskite oxides, crystallized in the ABO_3 structure (Fig. 1(a)), where the A-site is occupied by alkaline-earth ions and the B-site by transition-metal ions, exhibit a wide range of collective phenomena — including giant magnetoresistance, multiferroicity, and metal–insulator transitions — arising from the coupling among charge, spin, lattice, and orbital degrees of freedom.[1–6] At perovskite-based oxide surfaces or interfaces, structural reconstruction plays a crucial role in determining the electronic and magnetic properties beyond bulk properties because subtle rearrangements of the atomic structure — such as octahedral tilts, rotations, and distortions — can drastically modify the band topology, orbital occupancy, and exchange interactions.[2,7–9] In particular, lattice reconstructions at heterointerfaces often relax polar discontinuities or strain mismatches, leading to emergent two-dimensional electron systems, interfacial magnetism, or unconventional superconductivity.[10–12] For example, orbital reconstruction at the $LaAlO_3/SrTiO_3$ interface gives rise to symmetry breaking and a quantum 2D electron gas,[10] while similar effects in correlated perovskites such as $LaNiO_3$ and $SrRuO_3$ can induce metal–insulator transitions and nontrivial magnetic textures.[13,14] Thus, atomic-scale reconstruction serves as an effective tuning knob for manipulating quantum states in correlated oxides, providing a versatile platform for designing emergent functionalities.

In $SrNbO_3$, the Nb ions provide $4d^1$ electrons, expected to yield electronic properties analogous to those of the $3d^1$ perovskite $SrVO_3$, including a thickness-driven metal-insulator transition from an insulating state below 2 ML to a non-Fermi-liquid behavior above 6 ML.[5,15] Such dimensional crossover phenomena may be a universal feature of isostructural 4d transition-metal oxides due to their comparable electronic configurations. Although 4d transition-metal ions generally exhibit stronger hybridization with oxygen, weaker on-site Coulomb interactions, and hence weaker electron correlations than their 3d counterparts, earlier studies observed higher resistivity in $SrNbO_3$ films, which was later clarified to originate from non-stoichiometry.[16]

Angle-resolved photoemission spectroscopy (ARPES) investigations of $SrNbO_3$ remain scarce, largely due to the challenges of synthesizing high-quality epitaxial films and the stringent surface requirements for *in-situ* measure-

†Corresponding author. E-mail: hang.li@iphy.ac.cn

© 2026 Chinese Physical Society and IOP Publishing Ltd. All rights, including for text and data mining, AI training, and similar technologies, are reserved.

ments. Recent advances in film growth techniques, however, have enabled the fabrication of high-quality $SrNbO_3$ thin films,[17,18] which have attracted attention as transparent conductors owing to their high electrical conductivity and optical transmittance.[19–21] ARPES measurements on these films have confirmed a band structure consistent with density functional theory (DFT) calculations.[22] Moreover, strain-induced lattice distortions can give rise to non-symmorphic symmetry protection of Dirac points in the electronic band structure, suggesting that distorted $SrNbO_3$ may host correlated Dirac semimetal states.[23–26] Nevertheless, direct spectroscopic verification of such topological transitions has yet to be achieved.

In this work, we employ pulsed laser epitaxy to synthesize atomically smooth, stoichiometrically controlled $SrNbO_3$ thin films and probe their electronic structures via *in-situ* ARPES. By controlling the oxygen content of the substrate, we observe a distinct evolution of the Fermi surface reconstruction — from a $\sqrt{2}\times\sqrt{2}R45^\circ$ modulation in films grown on oxygen-deficient $SrTiO_3$ substrates to a 2×2 Fermi surface reconstruction in films on stoichiometric substrates. Furthermore, controlled variation of film thickness reveals the gradual suppression of the electron-like Fermi pocket at the M point, which might be associated with the relaxation of the $a^0a^0c^+$ lattice distortion driven by interfacial strain from the $SrTiO_3$ substrate. These results demonstrate that both chemical stoichiometry and thin film thickness provide effective tuning parameters for band reconstruction in correlated oxides, establishing $SrNbO_3$ as a versatile platform for engineering the interplay between topology, correlation, and dimensional confinement.

2. Result

$SrNbO_3$ thin films with thicknesses ranging from 1–200 ML were grown on $SrTiO_3$ substrates by pulsed laser deposition (PLD) to investigate the influence of epitaxial strain ($\varepsilon = -3.02\%$) on their structural and electronic properties. All films were grown under high-vacuum conditions. Despite the substantial lattice mismatch, high-quality films with atomically smooth surfaces were obtained, as evidenced by the x-ray diffraction (XRD) results shown in Fig. 1(b). The diffraction peaks corresponding to the (100) and (200) reflections of $SrNbO_3$ shift progressively toward larger angles with increasing thickness, indicating a reduction of the out-of-plane lattice constant c. We performed reciprocal space mapping (RSM) measurements on the (103) reflections of $SrNbO_3$ thin films with thicknesses ranging from 7 ML to 200 ML, as shown in Fig. 1(b). The (103) reflection intensities are relatively weak for ultrathin films (7 ML and 8 ML). Analysis of the RSM data reveals that the in-plane lattice constant a of $SrNbO_3$ increases progressively with film thickness, from approximately 3.921 Å at 7 ML to 3.987 Å at 200 ML. For thinner films, the in-plane lattice constant closely matches that of the $SrTiO_3$ substrate, whereas for thicker films, it approaches the bulk value of $SrNbO_3$. These complementary observations consistently point to a gradual relaxation of the epitaxial strain with increasing thickness. The behavior originates from the compressive in-plane strain imposed by the smaller lattice constant of the $SrTiO_3$ substrate, which initially elongates the lattice along the out-of-plane direction. As the film thickens, strain relaxation progressively restores both lattice parameters toward their bulk values, in agreement with the systematic peak shifts observed in XRD and RSM.

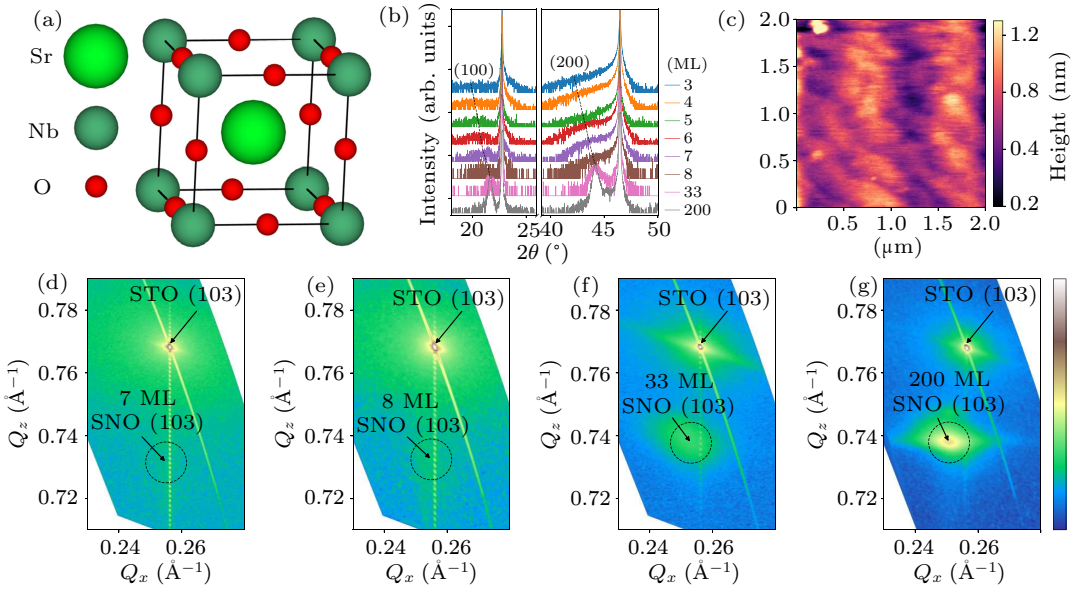


Fig. 1. Crystal structure, XRD and AFM of $SrNbO_3$ thin film. (a) The crystal structure of $SrNbO_3$. (b) The XRD test results of thin films with thickness ranging from 3–33 ML. It can be clearly seen from the figures that the peak positions of (100) and (200) shift towards higher angles with increasing film thickness. (c) The AFM test image of an 8 ML thick $SrNbO_3$ thin film, where we can clearly see relatively flat terraces, confirming that the film surface is atomically smooth. (d)–(g) The RSM of the (103) reflections for $SrNbO_3$ thin films with different thicknesses. In the figures, STO and SNO denote $SrTiO_3$ and $SrNbO_3$, respectively.

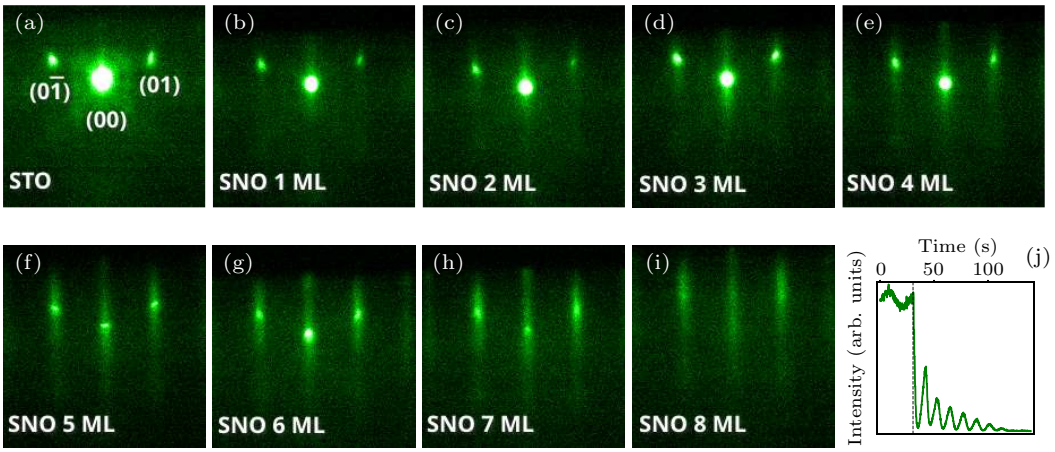


Fig. 2. RHEED images of $SrTiO_3$ substrate and $SrNbO_3$ thin films with different thicknesses. (a) The RHEED image of the $SrTiO_3$ thin film after being treated at 950 °C. The smooth circular spots suggest a flat substrate surface. (b)–(i) The RHEED images of $SrNbO_3$ thin films with thicknesses ranging from 1–8 ML. (j) The intensity of the central spot changing over time during 8 ML film growth, exhibiting seven peaks during growth.

The atomic force microscopy (AFM) image of an 8 ML film (Fig. 1(c)) reveals well-defined terraces, confirming the atomically flat surface morphology suitable for surface-sensitive ARPES measurements. Figure 2 shows reflection high-energy electron diffraction (RHEED) images of thin films with different thicknesses. The RHEED patterns for films with thicknesses less than 8 ML are significantly different from those with thicknesses greater than or equal to 8 ML. As the film thickness increases, the brightness of the central spot (00) gradually decreases until it disappears, as shown in Fig. 2, which is related to a progressive roughening of the surface, and the (01) spot remains, suggesting the preserved surface periodicity. This is consistent with the changes in the RHEED intensity of the central spot (00) recorded during growth (Fig. 2(j)), where seven peaks can be clearly observed, with peak intensities gradually decreasing. The RHEED oscillations confirm a layer-by-layer growth mode during the initial stages of deposition. The disappearance of these oscillations after the deposition of 7 ML indicates a transition to a different growth regime, such as step-flow or three-dimensional island growth, suggesting that the overall growth follows the Stranski–Krastanov mode.

$SrNbO_3$ has one electron occupying the Nb 4d states, which is distributed among the three nearly degenerate t_{2g} orbitals. Each orbital contributes a cylindrical Fermi surface sheet oriented along a principal axis. The band derived from the d_{xy} orbital exhibits no dispersion along the k_z direction, i.e., it is quasi-two-dimensional in nature.[22] To probe the electronic structure of $SrNbO_3$ films, we performed *in-situ* ARPES measurements on samples with varying thicknesses. The He II discharge line ($h\nu = 40.81$ eV) was used as the photon source, and the sample temperature was maintained below 100 K during the measurements. To fully map the three-dimensional electronic structure, photon-energy-dependent measurements would be required, as a single photon energy corresponds to a fixed k_z plane in the Brillouin zone. However, such measurements are not accessible with our fixed-energy He II source.

For films thicker than 3 ML, a circular electron pocket centered at the $\overline{\Gamma}$ point is observed, originating from the d_{xy} orbital of $SrNbO_3$. An additional pocket appears at the $\overline{M}$ point, corresponding to the folded Fermi surface at $\overline{\Gamma}$ induced by the $\sqrt{2} \times \sqrt{2}R45°$ Fermi surface reconstruction. With increasing thickness up to 7 ML, the spectral weight of the $\overline{M}$-point pocket enhances, reflecting improved crystallinity. At 8 ML, the pocket at $\overline{M}$ vanishes abruptly. For the 200 ML film, the band structure becomes identical to that of bulk $SrNbO_3$. The electron-like Fermi pockets expand progressively with increasing film thickness, as evidenced by the momentum distribution curves (MDCs) at E_F for films with different thicknesses shown in Fig. 3(g), as well as the mapping result at $E - E_F = -0.1$ eV in Fig. 3(c). This band reconstruction may originate from compressive-strain-induced $a^0a^0c^+$ octahedral rotations (Fig. 5(b)).[27–29] In the Glazer notation,[30] a^0 and c^+ denote the absence of rotation and in-phase rotation of the oxygen octahedra about the corresponding crystallographic axes, respectively. Such symmetry lowering folds the d_{xy}-derived band from the Γ point to M, leading to hybridization at the Brillouin zone boundary that is absent in the cubic $a^0a^0a^0$ phase (Figs. 5(a), 5(c) and 5(d)). The disappearance of the $\overline{M}$-point pocket at 8 ML is not likely due to the k_z dispersion of the band. Although thinner films are expected to exhibit larger k_z broadening, the electron pocket at the $\overline{M}$ and $\overline{\Gamma}$ points is derived from the d_{xy} orbital, which is quasi-two-dimensional in nature and has been verified experimentally to be detectable across all k_z planes in $SrNbO_3$ and similar perovskite $SrTiO_3$.[31,32] Therefore, the disappearance of the $\overline{M}$-point pocket is attributed to thickness-dependent effects rather than k_z-related broadening. From the XRD/RSM results, we observe a change in the lattice constant with increasing film thickness, indicating relaxation of the epitaxial strain. This suggests that the disappearance of the $\overline{M}$-point pocket at 8 ML

may be associated with the relaxation of the $a^0a^0c^+$ octahedral rotation. However, confirmation of the $a^0a^0c^+$ distortion requires further investigation. Such subtle structural modulations are difficult to detect using our two-stage differentially pumped RHEED due to their weak diffraction features, and high-resolution synchrotron XRD also remains challenging for ultrathin films owing to the limited scattering volume, compounded by the scarcity of beamtime access. Figures 3(d) and 3(h) display the ARPES intensity maps centered at the $\overline{\Gamma}$ and $\overline{M}$ points, respectively, for a 4 ML film. At this photon energy, the spectral weight primarily arises from the d_{xy} orbital, while the d_{xz} and d_{yz} contributions remain weak.

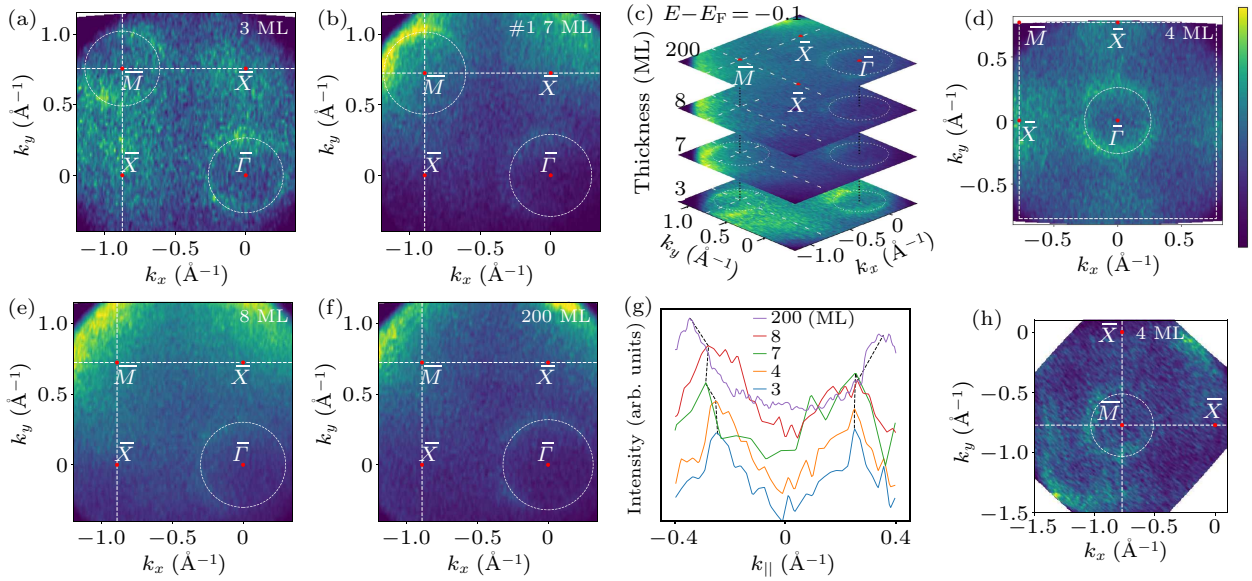


Fig. 3. Fermi surface patterns of $SrNbO_3$ thin films with different thicknesses. Panels (a), (b), (e) and (f) present the Fermi surfaces for films with thicknesses of 3 ML, 7 ML, 8 ML, and 200 ML, respectively. The Brillouin zone boundaries are marked by white dashed lines. (c) The band structures at binding energies of 0.1 eV below the Fermi level for $SrNbO_3$ films of varying thicknesses. (c) The MDCs at E_F for films with different thicknesses, along the $\overline{\Gamma}$–$\overline{X}$ direction. (d) and (h) The mappings centered at the $\overline{\Gamma}$ and $\overline{M}$ points for the 4 ML-thick film.

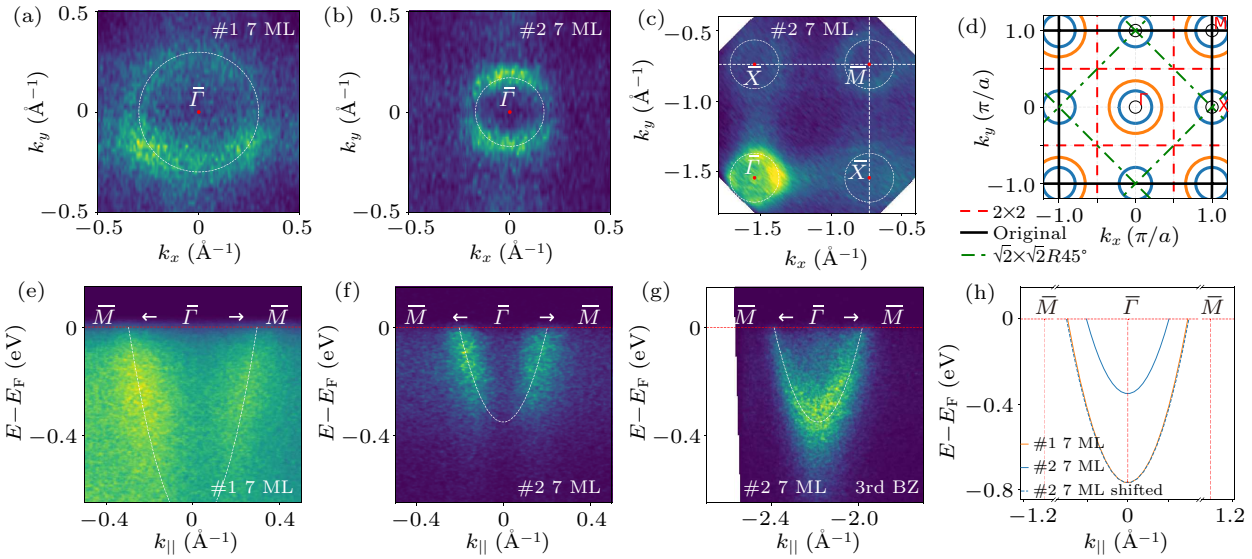


Fig. 4. Both (a) and (b) present ARPES mapping measurements centered at the $\overline{\Gamma}$ point for 7 ML $SrNbO_3$ thin films. The key distinction lies in the substrate condition: (a) corresponds to a film grown on an oxygen-deficient $SrTiO_3$ substrate, while (b) was deposited on a stoichiometric $SrTiO_3$ substrate. Panel (d) compares the Fermi surfaces extracted from the two samples, with the black curve representing the original Fermi surface, the blue curve representing the oxygen-deficient substrate $\sqrt{2}\times\sqrt{2}R45°$ Fermi surface and the orange curve denoting the stoichiometric 2×2 Fermi surface case. (c) The mapping result measured in the third Brillouin zone for the film on the stoichiometric substrate. (e) and (f) The band structures along the $\overline{\Gamma}$–$\overline{M}$ direction for the oxygen-deficient and stoichiometric substrates, respectively. (h) A direct comparison of the fitted band parameters derived from the $\overline{\Gamma}$–$\overline{M}$ direction. (g) The band structure along the $\overline{\Gamma}$–$\overline{M}$ direction measured in the third Brillouin zone.

Figures 4(a) and 4(b) show ARPES maps at the $\overline{\Gamma}$ point for 7 ML $SrNbO_3$ films grown on oxygen-deficient and stoichiometric $SrTiO_3$ substrates, hereafter denoted as samples #1 and #2, respectively. In Appendix A, we describe how the oxygen-deficient and stoichiometric substrates were prepared. The Fermi wave vector k_F of sample #1 is notably larger, indicating a higher carrier density due to oxygen deficiency. Figure 4(c) displays the third Brillouin zone map for sample #2,

revealing a distinct Fermi surface reconstruction pattern compared with sample #1. The oxygen-deficient substrate induces a $\sqrt{2}\times\sqrt{2}R45^\circ$ Fermi surface reconstruction possibly associated with the $a^0a^0c^+$ octahedral rotation (Fig. 5(d)), whereas the stoichiometric substrate leads to a 2×2 Fermi surface reconstruction. As a result, folded electron-like bands emerge at both the X and M points. The extracted Fermi surfaces are outlined in Fig. 4(d), where only the d_{xy} component is shown for clarity. This Fermi surface reconstruction cannot be attributed to the k_z dispersion of the band either, given that the d_{xy}-derived band is quasi-two-dimensional. We cannot attribute it to surface reconstruction, since our RHEED shows no evidence of surface reconstruction. There are some other possible effects related to the Fermi surface reconstruction, such as charge density wave and spin density wave.[33–35] The origin of the Fermi surface reconstruction here needs further investigation in the future. Figures 4(e) and 4(f) compare the band dispersions along $\overline{\Gamma}$–$\overline{M}$. In sample #2, the band bottom, invisible in the first Brillouin zone, becomes evident in the third (Fig. 4(g)). The effective mass ratios $r = m^*/m_e$ are nearly identical for the two films (0.436 and 0.452), consistent with the reported value of 0.46 in Ref. [22], and much smaller than $r_{GSO} \approx 1.7$ for $SrMoO_3$ on $GdScO_3$.[36] Although oxygen deficiency shifts the Fermi level upward and leaves the effective mass essentially unchanged, it results in markedly different Fermi surface reconstruction patterns.

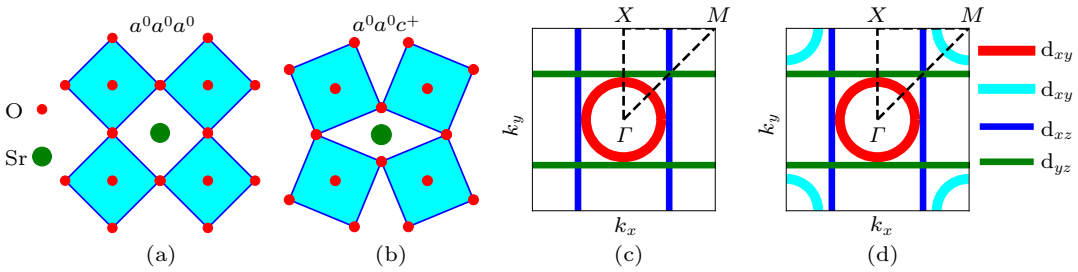


Fig. 5. Octahedral rotation modes and Fermi surface evolution in $SrNbO_3$. (a) Cubic phase ($a^0a^0a^0$, no rotation) and (b) strained phase ($a^0a^0c^+$ in-phase rotation) with corresponding (c) and (d) Γ–X–M plane Fermi surfaces. The $a^0a^0c^+$ symmetry induces Brillouin zone folding, modifying the original cubic Fermi surface topology (c) through zone-boundary band hybridization (d). The Fermi surfaces derived from the d_{xz} and d_{yz} bands are represented by the blue and green contours, respectively. The original d_{xy} band is depicted by the red contour, while the cyan contour arises from band folding.

3. Conclusions

In this study, we investigated the thickness-dependent electronic structure of $SrNbO_3$ films using ARPES. Pronounced spectral features emerge at a thickness of 3 ML, where clear electron-like bands appear at the $\overline{M}$ point, originating from band folding. These folded states persist up to 7 ML, but vanish once the thickness exceeds 8 ML. This evolution parallels the strain relaxation behavior, establishing a link between epitaxial strain, lattice reconstruction, and electronic topology. Specifically, the substrate-imposed strain — compressive for $SrTiO_3$ and tensile for $DyScO_3$ — defines a tunable electronic landscape where quantum confinement and strain jointly govern the emergent band structure. The critical thicknesses identified here, 3 ML for the onset of coherent spectral weight and 8 ML for the disappearance of folded bands, may signify distinct stages of strain accommodation and electronic reconstruction. Such thickness-dependent evolution from a correlated Dirac semimetal-like state to a more conventional metallic phase highlights the potential of 4d oxides as a platform for realizing strain-engineered quantum phase transitions, with implications for topological and quantum device design.

Furthermore, films grown on stoichiometric substrates exhibit a 2×2 Fermi surface reconstruction, distinct from the $\sqrt{2}\times\sqrt{2}R45^\circ$ pattern associated with the $a^0a^0c^+$ rotational distortion induced by oxygen-deficient substrates. Because of the limited photon energy range of the laboratory light source, our measurements predominantly probe the d_{xy}-derived states, whereas the d_{xz} and d_{yz} contributions remain too weak for reliable identification. Consequently, possible quantum-well subband features could not be resolved. Future synchrotron-based ARPES studies with tunable photon energies will be essential to fully map the orbital-selective band evolution and to clarify the role of confinement in modulating the correlated electronic states of $SrNbO_3$.

Appendxi A: Methods

A1. Pulsed laser deposition

We utilized a $SrTiO_3$ substrate with a CryTec (001) orientation. The substrate was pre-annealed at 600 °C for 30 min in the growth chamber for degassing. Once the vacuum state stabilized, the temperature was raised to 950 °C for an additional 30 min to obtain a $SrTiO_3$ substrate with a TiO_2-termination, which is referred to as the oxygen-deficient substrate in the main text. The stoichiometric $SrTiO_3$ was obtained by annealing at 500 °C for 30 min under an O_2 atmosphere at a pressure of 0.1 mbar. A KrF excimer laser ($\lambda = 248$ nm) was used to ablate the $Sr_2Nb_2O_7$ target material with a laser frequency of 2 Hz. Growth was performed directly in an ultra-high vacuum (UHV) environment, with the optimal substrate temperature for growth being 770 °C. The film thickness was monitored *in-situ* using RHEED, with clear oscillation signals observed

when the thickness was below 7 ML. Surface morphology was determined using AFM.

A2. Angle-resolved photoemission spectroscopy

All the ARPES data were collected at the Synergetic Extreme Condition User Facility (SECUF), using a Scienta Omicron DA30 electron analyzer with energy and angular resolutions better than 5 meV and 0.1°. The data were collected with helium discharge lamp light at a photon energy of He II 40.81 eV. The samples were measured *in-situ* via a high-vacuum transfer line from the PLD chamber under a base pressure better than 5×10^{-11} mbar.

Acknowledgements

The authors thank Dr. Meng Meng for his help on the film growth. This work is supported by the National Key R&D Program of China (Grant Nos. 2023YFA1406100 and 2022YFA1403800), the National Natural Science Foundation of China (Grant No. U1832202), and the Chinese Academy of Sciences (Grant No. XDB33000000). Most part of this work was carried out at Synergetic Extreme Condition User Facility (SECUF).

References

[1] Wolfram T and Ellialtioglu S 2006 *Electronic and Optical Properties of D-Band Perovskites* (Cambridge: Cambridge University Press)
[2] Hwang H Y, Iwasa Y, Kawasaki M, Keimer B, Nagaosa N and Tokura Y 2012 *Nat. Mater.* **11** 103
[3] Stranks S D and Snaith H J 2015 *Nat. Nanotechnol.* **10** 391
[4] Li J, Chen Y, Gong N, Huang X, Yang Z and Weng Y 2024 *Chin. Phys. B* **33** 017502
[5] Yoshimatsu K, Okabe T, Kumigashira H, Okamoto S, Aizaki S, Fujimori A and Oshima M 2010 *Phys. Rev. Lett.* **104** 147601
[6] Chen S X, Chen M M, Liu Y, Cao D W and Chen G J 2024 *Chin. Phys. B* **33** 098701
[7] Zubko P, Gariglio S, Gabay M, Ghosez P and Triscone J M 2011 *Annual Review of Condensed Matter Physics* **2** 141
[8] Rondinelli J M and Fennie C J 2012 *Adv. Mater.* **24** 1961
[9] Ok J M, Mohanta N, Zhang J, Yoon S, Okamoto S, Choi E S, Zhou H, Briggeman M, Irvin P, Lupini A R, Pai Y Y, Skoropata E, Sohn C, Li H, Miao H, Lawrie B, Choi W S, Eres G, Levy J and Lee H N 2021 *Sci. Adv.* **7** eabf9631
[10] Ohtomo A and Hwang H Y 2004 *Nature* **427** 423
[11] Reyren N, Thiel S, Caviglia A D, Kourkoutis L F, Hammerl G, Richter C, Schneider C W, Kopp T, Rüetschi A S, Jaccard D, Gabay M, Muller D A, Triscone J M and Mannhart J 2007 *Science* **317** 1196
[12] Chakhalian J, Freeland J W, Habermeier H U, Cristiani G, Khaliullin G, van Veenendaal M and Keimer B 2007 *Science* **318** 1114
[13] Liu J 2011 *Phys. Rev. B* **83** 161102(R)
[14] Grutter A J 2013 *Phys. Rev. Lett.* **111** 087202
[15] Kobayashi M, Yoshimatsu K, Mitsuhashi T, Kitamura M, Sakai E, Yukawa R, Minohara M, Fujimori A, Horiba K and Kumigashira H 2017 *Scientific Reports* **7** 16621
[16] Oka D, Hirose Y, Nakao S, Fukumura T and Hasegawa T 2015 *Phys. Rev. B* **92** 205102
[17] Balasubramaniam K R, Cao Y, Patel N, Havelia S, Cox P J, Devlin E C, Yu E P, Close B J, Woodward P M and Salvador P A 2008 *Journal of Solid State Chemistry* **181** 705
[18] Chen C, Lv S, Wang Z, Akagi K, Lichtenberg F, Ikuhara Y and Bednorz J G 2014 *Appl. Phys. Lett.* **105** 221602
[19] Mirjolet M, Kataja M, Hakala T K, Komissinskiy P, Alff L, Herranz G and Fontcuberta J 2021 *Adv. Opt. Mater.* **9** 2100520
[20] Jeong J, Kang B, Song J, Lee S, Kim C H, Choi U, Ko E K, Lee J H, Lee H T, Park H R, Lee J H, Kim M, Noh T W and Sohn C 2024 *Journal of the European Ceramic Society* **44** 6764
[21] Kumar S, Ahammad J, Das D, Kumar R, Dhar S and Johari P 2024 *J. Appl. Phys.* **135** 015303
[22] Bigi C, Orgiani P, Sławińska J, Fujii J, Irvine J T, Picozzi S, Panaccione G, Vobornik I, Rossi G, Payne D and Borgatti F 2020 *Phys. Rev. Mater.* **4** 025006
[23] Yao M Y, Zhu F, Han C Q, Guan D D, Liu C, Qian D and Jia J F 2016 *Scientific Reports* **6** 21326
[24] Vistoli L, Wang W, Sander A, Zhu Q, Casals B, Cichelero R, Barthélémy A, Fusil S, Herranz G, Valencia S, Abrudan R, Weschke E, Nakazawa K, Kohno H, Santamaria J, Wu W, Garcia V and Bibes M 2019 *Nat. Phys.* **15** 67
[25] Li S, Lin Z, Hu W, Yan D, Chen F, Bai X, Zhu B, Yuan J, Shi Y, Jin K, Weng H and Guo H 2023 *Chin. Phys. B* **32** 047103
[26] Lygo A C, Guo B, Rashidi A, Huang V, Cuadros-Romero P and Stemmer S 2023 *Phys. Rev. Lett.* **130** 046201
[27] Chikina A, Rosendal V, Li H, Guedes E B, Caputo M, Plumb N C, Shi M, Petersen D H, Brandbyge M, Brito W H, Pomjakushina E, Scagnoli V, Lyu J, Medarde M, Skoropata E, Staub U, Huang S W, Baumberger F, Pryds N and Radovic M 2023 (*Preprint* 2311.06072)
[28] Rosendal V, Brito W H, Radovic M, Chikina A, Brandbyge M, Pryds N and Petersen D H 2023 *Phys. Rev. Mater.* **7** 075002
[29] Chikina A, Rosendal V, Li H, Skoropata E, Guedes E B, Caputo M, Plumb N C, Shi M, Petersen D H, Brandbyge M, Brito W H, Pomjakushina E, Scagnoli V, Lyu J, Medarde M, Staub U, Huang S W, Múller Gubler E A, Baumberger F, Pryds N and Radovic M 2025 *Phys. Rev. B* **111** 155146
[30] Glazer A M 1972 *Acta Crystallographica Section B Structural Crystallography and Crystal Chemistry* **28** 3384
[31] Plumb N C, Salluzzo M, Razzoli E, Månsson M, Falub M, Krempasky J, Matt C E, Chang J, Schulte M, Braun J, Ebert H, Minár J, Delley B, Zhou K J, Schmitt T, Shi M, Mesot J, Patthey L and Radović M 2014 *Phys. Rev. Lett.* **113** 086801
[32] Li H, Yun S, Chikina A, Rosendal V, Tran T, Brand E, Christoffersen C H, Plumb N C, Shi M, Pryds N and Radovic M 2024 *Advanced Functional Materials* **34** 2313236
[33] Rossnagel K, Rotenberg E, Koh H, Smith N V and Kipp L 2005 *Phys. Rev. B* **72** 121103
[34] Yang L X, Zhang Y, Ou H W, Zhao J F, Shen D W, Zhou B, Wei J, Chen F, Xu M, He C, Chen Y, Wang Z D, Wang X F, Wu T, Wu G, Chen X H, Arita M, Shimada K, Taniguchi M, Lu Z Y, Xiang T and Feng D L 2009 *Phys. Rev. Lett.* **102** 107002
[35] Yang R, Huang J W, Zaki N, Pletikosić I, Dai Y M, Xiao H, Valla T, Johnson P D, Zhou X J, Qiu X G and Homes C C 2019 *Phys. Rev. B* **100** 235132
[36] Cappelli E, Hampel A, Chikina A, Guedes E B, Gatti G, Hunter A, Issing J, Biskup N, Varela M, Dreyer C E, Tamai A, Georges A, Bruno F Y, Radovic M and Baumberger F 2022 *Phys. Rev. Mater.* **6** 075002